Journal of Marine Research, 70, 141–172, 2012

Cross-shelf mixing and mid-shelf front dynamics in the Mid-Atlantic Bight evaluated using the radium quartet

by Scott L. Stachelhaus[1,2], S. Bradley Moran[1], David S. Ullman[1] and Roger P. Kelly[1]

ABSTRACT

Mid-shelf fronts (MSFs) are thought to be ubiquitous in shelf areas. However, their dynamical role in cross-shelf mixing has yet to be fully characterized. In January, February, and April of 2007, radium isotopes (^{223}Ra, $t_{1/2} = 11$ d; ^{224}Ra, $t_{1/2} = 3.7$ d; ^{226}Ra, $t_{1/2} = 1600$ yr; ^{228}Ra, $t_{1/2} = 5.7$ yr) were measured along a transect in the Mid-Atlantic Bight to constrain mixing rates at and around a MSF. Cross-shelf eddy diffusivities (K_x) were determined from ^{223}Ra and ^{224}Ra distributions using a variable-depth model. Two key assumptions – minimal advection and negligible benthic radium input – involving the use of ^{223}Ra and ^{224}Ra as tracers of mixing were quantitatively evaluated in order to assess the accuracy of the K_x estimates. Eddy diffusivities over the three-month sampling period range from $0.1 \pm 0.05 - 1.6 \pm 0.5 \times 10^2$ m^2 s^{-1} for ^{223}Ra and from $1.7 \pm 0.4 - 2.2 \pm 0.6 \times 10^2$ m^2 s^{-1} for ^{224}Ra. The temporal variability in K_x is low in comparison to the uncertainty of the derived values, indicating that eddy diffusivity in this area is relatively constant throughout the sampling period. Observations in the Mid-Atlantic Bight differ from theoretical data corresponding to the tidal dispersion frontogenesis model, suggesting that a different mechanism is responsible for MSF formation. Variability in supported ^{223}Ra and ^{228}Ra observed near the front indicates that cross-shelf mixing may be inhibited by MSFs. Conversely, along-shelf transport is enhanced by the front's presence. These results indicate that the equatorward jet associated with the front is capable of effectively transporting dissolved chemicals over hundreds of kilometers.

1. Introduction

Fronts, defined as narrow zones of sharp property gradients (Belkin and Spall, 2002), play a significant role in ocean dynamics. These features are often linked with strong vertical (Houghton and Visbeck, 1998) and horizontal (Tintore *et al.*, 1988) velocities, and can inhibit cross-shelf mixing (e.g. Blanton, 1986; Linden and Simpson, 1988; Hill *et al.*, 1993). Fronts influence the distribution of nutrients, pollutants, and biology ranging in size from phytoplankton to marine mammals; previous observations have revealed that fronts can be associated with maxima for primary production (e.g. Marra *et al.*, 1990; Laubscher *et al.*, 1993; Yoder *et al.*, 1994). Although mid-shelf fronts (MSFs) are thought to be ubiquitous,

1. Graduate School of Oceanography, University of Rhode Island, Narragansett, Rhode Island, 02882, U.S.A.
2. Present address. St. George's School, Middletown, Rhode Island, 02842, U.S.A. ***email: scott_stachelhaus@stgeorges.edu***

their vertical structure, formation mechanism, and effect on cross-shelf mixing are poorly understood. An assessment of how MSFs influence cross-shelf mixing is important in adding to the understanding of how heat, salt, and dissolved constituents are exchanged between coastal waters and the open ocean.

Eddy diffusion is one of the primary mechanisms contributing to cross-shelf mixing. Many methods, each with their own benefits and drawbacks, have been employed to evaluate eddy diffusion, including hydrodynamic models (e.g. Harms *et al.*, 2000; Perlanez, 2004; Wu *et al.*, 2005), passive drifters (e.g. List *et al.*, 1990; Münchow and Garvine, 1993; Ullman *et al.*, 2006), chemical dyes (e.g. Okubo, 1971; Sundermeyer and Ledwell, 2001), and natural tracers (e.g. Imboden and Emerson, 1978; Moore, 2000). The radium quartet (^{223}Ra, $t_{1/2} = 11$ d; ^{224}Ra, $t_{1/2} = 3.7$ d; ^{226}Ra, $t_{1/2} = 1600$ yr; ^{228}Ra, $t_{1/2} = 5.7$ yr), in particular, is well-suited as a tracer for mixing, due to its coastal source, near-conservative behavior in saline water, and wide range in half-lives. However, there still are a number of important assumptions inherent to most radium-based mixing models, including negligible advection and benthic input, which must be addressed in order to ensure the accuracy of this approach.

In this study, mixing in the vicinity of a MSF in the Mid-Atlantic Bight (MAB) is evaluated using radium isotopes. Cross-shelf eddy diffusivities are estimated from ^{223}Ra and ^{224}Ra distributions using constant-depth and variable-depth models. A quantitative analysis of the uncertainties in these estimates is provided, and two major assumptions (insignificant advection and minimal benthic radium input) in the application of the radium models are evaluated using nondimensional scaling. Radium-based diffusivities from this study are compared to values determined for the MAB using other methods; this comparison is extended to a discussion of eddy diffusivity's temporal variability in this region. Finally, the role of MSFs in cross-shelf mixing and the jet transport associated with these features is addressed in the context of radium isotope distributions.

2. Methods

a. Study area

The MAB encompasses an area of the continental margin off the eastern coast of the United States that extends from Massachusetts to North Carolina. The largest freshwater inputs to the region originate from the Connecticut, Hudson, Delaware, and Chesapeake rivers. Shelf water comprises the bulk of all water in the Bight; this water mass is cooler and less saline than the slope water originating offshore of the continental shelf area (Mountain, 2003). Mean flow along the shelf is to the southwest, and is part of a buoyancy-driven current originating offshore of southern Greenland (Chapman and Beardsley, 1989). While freshwater over the majority of the MAB shelf ultimately is derived from the Arctic, it has been hypothesized that the inner shelf is heavily influenced by local buoyancy sources (Ullman and Cornillon, 2001).

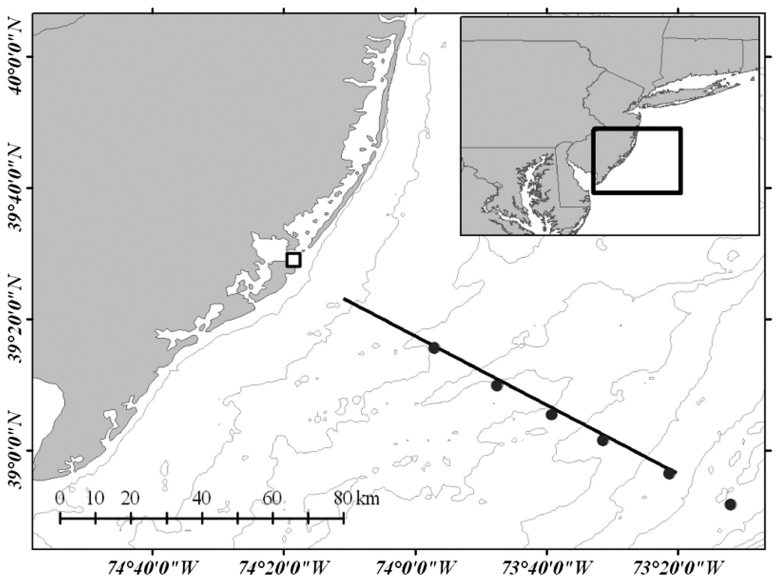

Figure 1. Map of study area showing cruise track. Surface samples were collected along the transect (black line) from 15 km to 120 km offshore of Great Bay, New Jersey (white square). Additional samples were collected from multiple depths at a series of stations (black dots) in the vicinity of the transect.

Previous work by Ullman and Cornillon (1999) identified a region of high frontal probability, distinct (in satellite data) from both shelf break and tidal mixing fronts, centered around the 50-meter isobath in the MAB. This MSF is present primarily during winter months. Although this feature was initially detected through its associated temperature gradient, changes in density across the feature are primarily linked to salinity. The front separates cool, freshwater near the coast from relatively warmer, saltier water offshore (Ullman and Cornillon, 2001).

b. Sample collection and analysis

In early 2007, an interdisciplinary study was undertaken in order to provide a comprehensive survey of a MSF located within the MAB. Hydrographic sampling was conducted along a radiator pattern and long line centered around an area of high frontal probability, located roughly 150 km south of the mouth of the Hudson River and offshore of Great Bay, New Jersey (Fig. 1). Radium samples were collected from the surface water on a 120-km transect across the front and from multiple depths at five CTD stations located along this line.

Field research was conducted aboard the *R/V Endeavor* during three separate cruises in January, February, and April of 2007. Surface water samples (∼200L) were collected using

the ship's seawater intake and were filtered through a 1-μm cartridge filter connected to the intake during collection in order to eliminate particulate matter. Sample volumes were determined using an in-line flow meter. Each surface sample was collected over a period of ~10 minutes while the ship continuously moved along the transect. Given an approximate velocity of 6–7 knots, individual samples cover a lateral distance of roughly 2 km. Unfiltered samples were also collected from multiple depths along the transect using a series of Niskin bottles mounted aboard a CTD rosette. Additional surface samples were collected at each CTD station using the ship's seawater intake; like the CTD samples, these were unfiltered, and were collected while the ship held its position at each CTD station. All seawater samples were temporarily stored in large plastic drums aboard the vessel. Immediately following collection, the samples were pumped from their containers and through cartridges containing Mn-impregnated acrylic fiber at rates of <1 L/min to extract dissolved Ra. The fiber samples were then partially dried with compressed air before analysis for ^{223}Ra and ^{224}Ra.

The fiber samples were measured for total dissolved ^{223}Ra and ^{224}Ra using a delayed-coincidence counter (RaDeCC) following the methods of Moore and Arnold (1996). Activities were measured across four separate detectors within a maximum of two weeks following collection; first counts were made in as little as 7 hours after collection. Each detector was calibrated using a mixed standard of known ^{223}Ra and ^{224}Ra activity. Average detector efficiencies were 0.5 ± 0.1 and 0.6 ± 0.1 for ^{223}Ra and ^{224}Ra, respectively. Samples were counted once on each detector, and uncertainty for ^{223}Ra and ^{224}Ra is expressed as the standard deviation of each sample's average activity across the four detectors. The average relative error was 42% for ^{223}Ra activity (range: 8–178%) and 22% for ^{224}Ra (range: $<1-121$%). Supported ^{224}Ra activities were also measured using this procedure after more than three weeks following collection. However, due to instrumental backlog, supported ^{224}Ra activities could not be quantified for the entire suite of samples. Supported ^{224}Ra activities were obtained for 45% of the samples collected in January, 53% of the samples collected in February, and 100% of the samples collected in April.

Following these initial measurements, the fiber samples were dried and combusted in a muffle furnace at 820°C for 16 hours and then packed into polystyrene vials at a roughly constant geometry and density. Each vial was capped with epoxy to prevent loss of ^{222}Rn and allowed to stand for a minimum of 20 days in order for ^{222}Rn to reach secular equilibrium with ^{226}Ra. ^{226}Ra and ^{228}Ra activities were then measured using a Canberra germanium well-type gamma spectrometer (active volume $= 154\,\text{cm}^3$). Each sample was counted to an uncertainty of $<10\%$ (1σ) for both isotopes. The detector was calibrated using a series of standards with appropriate geometries.

Temperature, salinity, and density data was acquired along the transect using a CTD attached to an undulating vehicle (Scanfish) towed behind the ship (Decker, 2009). Additional CTD data was obtained alongside the unfiltered radium samples collected at various depths along the transect.

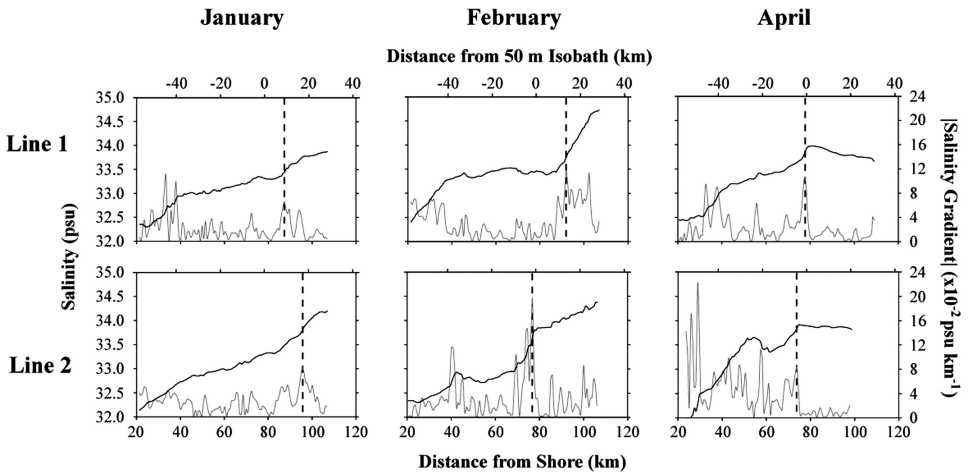

Figure 2. Salinity (black line) and salinity gradient (gray line) data measured at 10 m depth along the long line transects. The dashed vertical black lines represent the MSF's instantaneous position during each transect.

3. Results

The MSF's position is defined as the location where the cross-shelf salinity gradient at 10 m depth is at a maximum (Decker, 2009). To ensure that the front identified using this criterion was, in fact, a MSF, only areas within 20 km of the 50-m isobath are considered here; other high-gradient areas were present closer to shore (Fig. 2). The front's position shifts over time, as illustrated by hydrodynamic data acquired over both the long line transects (Fig. 2) and depth sections (Fig. 3). During January, the MSF is located between 87–96 km from shore (9–18 km offshore of the 50-m isobath), moving offshore over the study period (Table 1). The front's position is more variable during February, shifting from 94 km from shore (16 km offshore of the 50-m isobath) on February 20 to 77 km from shore (1 km inshore of the 50-m isobath) on February 27. In April, the front is consistently located close to the 50-m isobath, ranging from 4 km inshore to 2 km offshore of this depth (74–80 km from shore). The front's strength, as defined by its density step and gradient, also varies throughout the three months. The MSF strengthens from January to February before weakening considerably in April (Table 2).

Activities of all four radium isotopes in the study area generally decrease with increasing distance from shore (Fig. 4). In January, surface total ^{224}Ra activity drops rapidly within 30 km from shore before leveling off at a value of $\sim$1.5 dpm 100L^{-1}. Surface total ^{223}Ra activities observed during January exhibit a slightly more complex pattern. In a similar manner to total ^{224}Ra, total ^{223}Ra activity decreases steeply within 40 km from shore before approaching a value of $\sim$0.11 dpm 100L^{-1}. Total ^{223}Ra decreases from 0.11 dpm 100L^{-1} to 0.05 dpm 100L^{-1} at roughly 75 km from shore. The latter activity is present throughout the

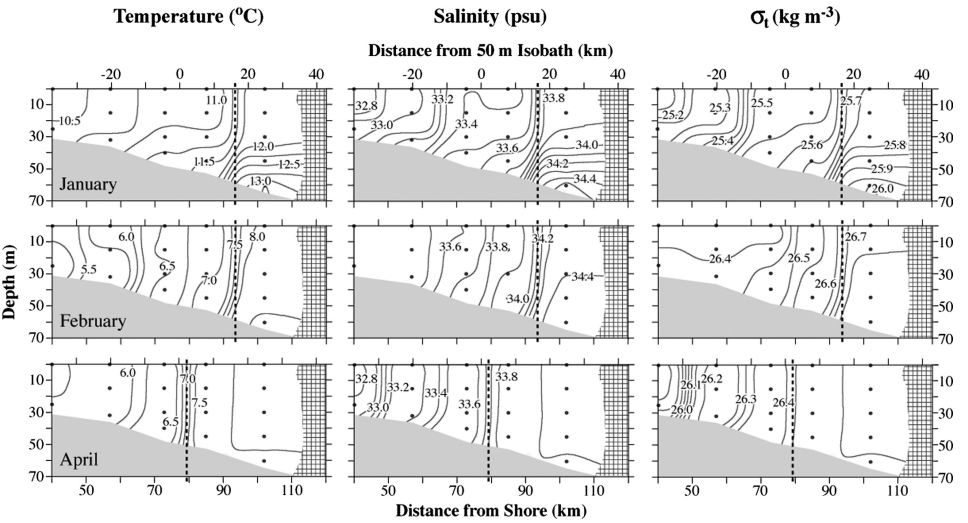

Figure 3. Depth sections of temperature, salinity, and density (σ_t). Sections were interpolated using Ocean Data View (v. 3.2.2.). The front's instantaneous position is depicted by the dashed vertical black lines. Cross-hatched areas represent regions with no data. CTD sampling stations are depicted using black dots.

Table 1. Instantaneous MSF position, determined by maximum salinity gradient at 10-m depth.

		MSF Position	
	Date	km from shore	km from 50-m isobath
January			
Line 1	1/12/07	87	9
Depth Section	1/13/07	94	16
Line 2	1/16/07	96	18
February			
Depth Section	2/20/07	94	16
Line 1	2/22/07	92	14
Line 2	2/27/07	77	−1[a]
April			
Line 1	4/4/07	78	0
Depth Section	4/6/07	80	2
Line 2	4/8/07	74	−4[a]

[a]Negative values reflect distances inshore of 50-m isobath.

remainder of the transect. The cross-shelf ^{228}Ra gradient is not consistent along the entire transect during this month; while the gradients between 0–45 km and 75–120 km from shore are similar (-0.10 dpm 100L^{-1} km^{-1}), the slope between 45–75 km from shore is

Table 2. Cruise-averaged frontal data (Decker, 2009).

	January	February	April
Location (distance relative to 50 m isobath, km)	6.5 ± 1.5	2.5 ± 1.7	-3.0 ± 1.2
Location (offshore distance, km)	84.3 ± 1.5	80.3 ± 1.7	74.8 ± 1.2
Density Step ($kg\,m^{-3}$)	0.118 ± 0.018	0.168 ± 0.013	0.055 ± 0.009
Density Gradient ($\times 10^{-3}\,kg\,m^{-3}\,km^{-1}$)	25 ± 2	51 ± 5	17 ± 3
Jet Velocity ($cm\,s^{-1}$)	6 ± 2	31 ± 2	9 ± 3

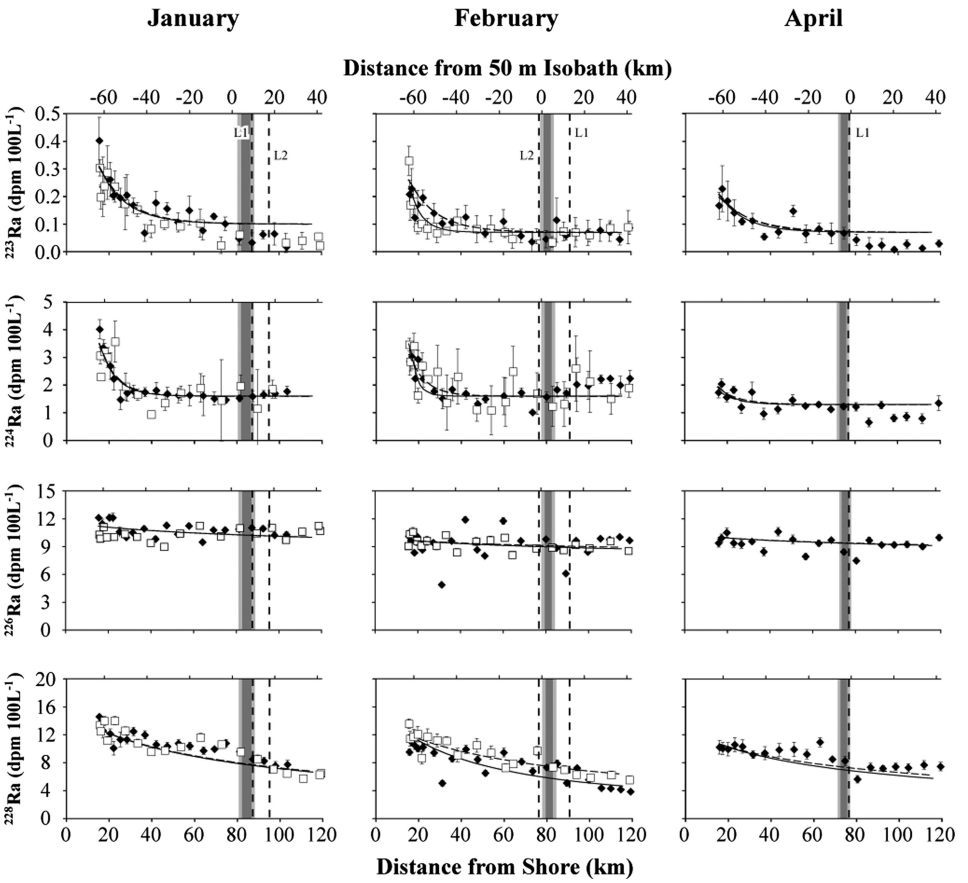

Figure 4. Plot of surface radium data. Closed and open symbols represent samples collected from the first and second lines, respectively, during each cruise. Error bars represent counting error (1σ). As with Figure 2, the vertical dashed black lines depict the front's instantaneous position during the first (L1) and second (L2) transects from each month. The front's cruise-averaged position (and average width) is represented using vertical dark gray bars, with its standard deviation shown using vertical light gray bars. Cruise-averaged frontal data is taken from Decker (2009). Lines through the data depict ^{223}Ra- (solid) and ^{224}Ra-based (dashed) K_x solutions based on the variable-depth model.

negligible, and may actually be slightly positive. Surface ^{226}Ra activity during this month exhibits a small (-0.01 dpm 100L^{-1} km^{-1}) linear gradient.

Both surface total ^{224}Ra and ^{223}Ra distributions observed in February are somewhat similar to those seen during January. Surface total ^{224}Ra and ^{223}Ra activities decrease rapidly within 30 km from shore before leveling off at values of 1.6 dpm 100L^{-1} and 0.11 dpm 100L^{-1}, respectively. Surface total ^{224}Ra remains at this level until 80 km from shore, where the isotope's activity then rises, eventually reaching a value of 2.3 dpm 100L^{-1} at 120 km from shore. Total ^{223}Ra values in the surface water drop to 0.05 dpm 100L^{-1} at 65 km from shore, before abruptly increasing to 0.07 dpm 100L^{-1} at 85 km from shore. Total ^{223}Ra activities in the surface water remain close to this level for the rest of the transect. While surface ^{228}Ra activity decreases with distance from shore, there is some difference in the ^{228}Ra distribution between the two lines. The ^{228}Ra gradient from line 1 observed between 94 and 105 km from shore (-0.3 dpm 100L^{-1} km^{-1}) is considerably steeper than that seen elsewhere along the transect (-0.04 dpm 100L^{-1} km^{-1}). The second line's ^{228}Ra data shows a similar pattern. In this case, the ^{228}Ra gradient between 85 and 96 km from shore (-0.1 dpm 100L^{-1} km^{-1}) is steeper than those from 15–85 km from shore (-0.06 dpm 100L^{-1} km^{-1}) and between 96 and 120 km from shore (-0.02 dpm 100L^{-1} km^{-1}). As in January, February surface ^{226}Ra decreases marginally (on the order of -0.01 dpm 100L^{-1} km^{-1}) with offshore distance in a linear fashion.

Only radium activity from the first transect across the front was used in April, as samples from the second transect showed signs of contamination from thorium in the ship's intake. Surface total ^{224}Ra inshore of 35 km is only slightly elevated above the average activity offshore of this location (1.1 dpm 100L^{-1}). As a result, the total ^{224}Ra gradient is difficult to discern. Surface total ^{223}Ra decreases from 0.23 dpm 100L^{-1} at 17 km from shore to a value of 0.07 dpm 100L^{-1} at 44 km from shore; it remains at this level until 74 km from shore. Between 74 and 86 km from shore, surface total ^{223}Ra activity drops from 0.07 to 0.02 dpm 100L^{-1}. The latter activity is roughly maintained (± 0.01 dpm 100L^{-1}) for the remainder of the line. Once again, the April ^{228}Ra gradient is not consistent over the transect. In this case, a sharper gradient exists between 15 and 36 km from shore (-0.04 dpm 100L^{-1} km^{-1}) and 60 and 80 km from shore (-0.13 dpm 100L^{-1} km^{-1}) than between 36–60 and 80–120 km from shore, where the gradient is negligible. Surface ^{226}Ra again decreases away from shore linearly on the order of -0.01 dpm 100L^{-1} km^{-1}.

Although the activity of all four radium isotopes exhibits some variability with depth (Fig. 5), there are, with some exceptions, few features consistent among the entire radium suite during any of the three cruises. Of note, elevated ^{226}Ra and ^{228}Ra activities are observed between 80 and 95 km from shore in January. These elevated activities are confined to the upper 15 m of the water column, and are not present to this degree anywhere else in the depth section. A similar pattern is present in February. However, while the elevated ^{226}Ra activity is still confined to between 80 and 95 km from shore, high ^{228}Ra activity stretches from 70 to 90 km from shore. The ^{228}Ra activity apex is also centered inshore of the highest ^{226}Ra concentrations. Moreover, elevated ^{228}Ra activity is also present near the seafloor

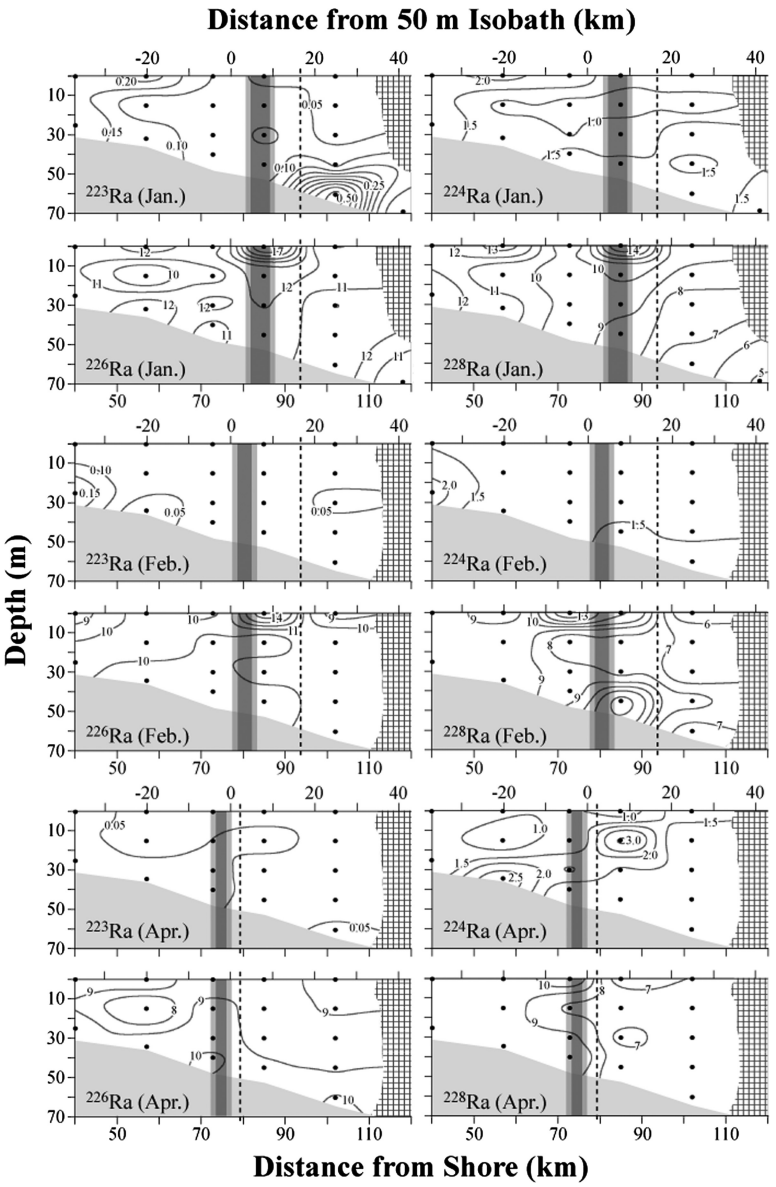

Figure 5. Radium isotope depth sections. Unfiltered radium samples were collected at discrete depths (black dots). In January and February, ^{226}Ra and ^{228}Ra are enriched in the surface water near the front. The front's instantaneous and cruise-averaged position are depicted using the same symbols as in Figure 4.

at 85 km from shore during this time. Elevated ^{226}Ra and ^{228}Ra activities are not evident during April.

Supported ^{224}Ra activities measured during each cruise do not show a distinct trend with respect to either offshore distance or water depth. Both January and February's average supported ^{224}Ra activities are 0.4 ± 0.2 dpm $100L^{-1}$. Supported ^{224}Ra activities observed in April are generally higher and more variable than those measured during the previous two cruises. The average supported ^{224}Ra activity in April is 0.8 ± 0.5 dpm $100L^{-1}$.

4. Discussion

a. Radium as a tracer for mixing: Theory

Radium isotopes have been recognized as tracers of mixing in the oceans for more than fifty years (e.g. Koczy, 1958). The primary source of radium is located at the coastline (in the form of desorption from sediments and particles, along with submarine groundwater discharge), and radium isotopes behave nearly conservatively following their release into the ocean. The distribution of a given radium isotope is primarily dependent upon the rate it is mixed away from shore and its respective half-life. Over the past several decades, many studies (e.g. Somayajulu *et al.*, 1996; Torgersen *et al.*, 1996; Moore, 2000, 2003; Rasmussen, 2003; Hancock *et al.*, 2006; Charette *et al.*, 2007; Colbert and Hammond, 2007; Peterson *et al.*, 2008) have employed radium isotopes to quantify coastal mixing rates, and, specifically, cross-shelf eddy diffusivities (K_x).

Cross-shelf gradients are, by and large, considerably larger than along-shelf gradients in dissolved radium activity. Given the assumption that radium activities are invariant with depth, the dissolved radium distribution on the shelf can be approximated using a one-dimensional model. In this manner, the change in a radium isotope's *unsupported* dissolved activity (A) over time (t) with respect to offshore distance (x) is expressed as follows (e.g. Hancock *et al.*, 2006):

$$\frac{\partial A}{\partial t} + \frac{1}{H}\frac{\partial}{\partial x}(uHA) = \frac{1}{H}\frac{\partial}{\partial x}\left(K_x H \frac{\partial A}{\partial x}\right) - \lambda A + \frac{B}{H}, \tag{1}$$

where H is depth, K_x is cross-shelf eddy diffusivity, u is cross-shelf velocity, λ is the isotope's decay constant, and B represents the benthic radium flux. As outlined by Moore (2000), if K_x is constant, advection and benthic input are insignificant, the water column is of constant depth, and the system is in steady state with respect to the radium isotope, Eq. (1) can be written as

$$0 = K_x \frac{\partial^2 A}{\partial x^2} - \lambda A. \tag{2}$$

In this case, the assumption of constant depth is conceptually equated to a constant-depth mixed layer. The solution to Eq. (2) (with boundary conditions $A = A_0$ at $x = 0$ and $A \to 0$ as $x \to \infty$) is an exponential equation,

$$A(x) = A_0 \exp\left(-x\sqrt{\frac{\lambda}{K_x}}\right). \tag{3}$$

Using this equation, eddy diffusivity can be estimated from a plot of radium activity against offshore distance. This approach has been used in the majority of radium-based eddy diffusion studies.

For a variable-depth water column (where all other assumptions are valid), however, the solution to Eq. (1) is different. In this case, Eq. (1) is expressed as:

$$0 = \frac{\partial^2 A}{\partial x^2} + \frac{1}{H}\frac{\partial H}{\partial x}\frac{\partial A}{\partial x} - \frac{\lambda A}{K_x}. \tag{4}$$

Previous studies (e.g. Hancock *et al.*, 2006; Lamontagne *et al.*, 2008) have obtained a radium-based K_x for a variable-depth water column by discretizing Eq. (4) and solving the equation using Gaussian elimination. K_x can also be determined using a modified Bessel function in a manner similar to the exponential model. If the ocean bottom is considered to have a linear slope α and depth at the coast H_0, an analytical solution to Eq. (4), given the same boundary conditions listed above, is

$$A_x = \frac{A_0}{K_0(\beta H_0)} K_0[\beta(H_0 + \alpha x)], \tag{5}$$

where

$$\beta = \sqrt{\frac{\lambda}{\alpha^2 K_x}}, \tag{6}$$

and K_0 represents a modified Bessel function of the second kind. As with Eq. (3), K_x can be estimated by fitting Eq. (5) to a plot of radium-versus-offshore distance.

b. Evaluation of major assumptions in the use of Ra isotopes as tracers of K_x

The assumption that diffusion and decay dominate the balance in Eq. (1) can be evaluated by developing a basic scale for each term in this equation. A generic variable p can be expressed as the product of a dimensionless number on the order of one and a scale term, such that

$$p = p^*\mathbf{p}, \tag{7}$$

where the starred term represents the dimensionless number and the bold term is the scale. Using this relation, the diffusion term, for example, can be transformed as follows:

$$\frac{1}{H}\frac{\partial}{\partial x}\left(K_x H \frac{\partial A}{\partial x}\right) = \frac{1}{H^*\mathbf{H}}\frac{\partial}{\partial x^*\mathbf{L}}\left(K^*\mathbf{K}H^*\mathbf{H}\frac{\partial A^*\mathbf{A}}{\partial x^*\mathbf{L}}\right) \approx \frac{\mathbf{KA}}{\mathbf{L}^2}, \tag{8}$$

where **L** is the length scale, which is equated with the e-folding distance for a given radium isotope's activity. The terms in Eq. (1) can consequently be scaled as:

$$\frac{\mathbf{A}}{\mathbf{T}} + \frac{\mathbf{UA}}{\mathbf{L}} \approx \frac{\mathbf{KA}}{\mathbf{L}^2} - \lambda\mathbf{A} + \frac{\mathbf{B}}{\mathbf{H}}. \tag{9}$$

The ratio of diffusion to advection can thus be expressed as **K/UL**, and that of diffusion to benthic input is $\mathbf{KAH/BL}^2$. The e-folding distance observed for both ^{223}Ra and ^{224}Ra in this study is on the order of 10 km. If the scale of cross-shelf diffusivity is approximately 2×10^2 m^2 s^{-1}, which falls in line with past K_x estimates made for the MAB (Stommel and Leetmaa, 1972; e.g. Münchow and Garvine, 1993; Ullman *et al.*, 2006), a cross-shelf velocity of only 2 cm s^{-1} is required for the advective term to be of equal magnitude to the diffusive term. Likewise, taking into account the range in ^{223}Ra activity ($\sim 0.1 - 0.4$ dpm 100L^{-1}), ^{224}Ra activity ($\sim$1.5–3.5 dpm 100L^{-1}) and water depth (20–30 m) over the area where discernible ^{223}Ra and ^{224}Ra gradients exist, benthic inputs of 4×10^{-5} dpm m^{-2} s^{-1} for ^{223}Ra and 6×10^{-4} dpm m^{-2} s^{-1} for ^{224}Ra would be sufficient to equal the diffusive term. Thus, even small amounts of advection and benthic radium input, if ignored, can lead to incorrect diffusivity estimates. In particular, offshore advection will yield an overestimate of K_x, while onshore advection and benthic input will produce underestimates of K_x.

Onshore and offshore advection can be achieved in several ways, and can introduce uncertainties into both models that assume a constant-depth mixed layer and those involving a well-mixed water column of variable depth. In coastal regions, upwelling (downwelling) can produce offshore (onshore) advection in the surface layer. This scenario is only problematic when the constant-depth mixed layer is taken into consideration, as flow in the surface layer is balanced by an opposing flow in the remaining water column. River discharge at the coast is also associated with net offshore advection because a compensating offshore flux is required to maintain the freshwater balance. Larger amounts of river discharge will lead to higher advective velocities. Net advection can occur over the entire water column even in the absence of freshwater input, due to the influence of winds and other forces. In this case, cross-shelf advection would necessitate either a corresponding along-shelf flow or sea level set-up in order to fulfill the continuity equation for incompressible flows.

Cross-shelf velocities of at least 2 cm s^{-1} are common in the MAB (e.g. Palmer and Lear, 1973; Rasmussen, 2003), and are likely not limited to the surface layer. Wang (1979) observed nontidal sea level set-up in the MAB, indicating net advection of water over the entire water column. Cross-shelf velocities measured during the three cruises have been reported by Decker (2009). In January, an upwelling system was observed, with offshore advection in the surface and onshore flow at the bottom. Cross-shelf velocities in the top 20 m of the water column during this month were between 2 and 4 cm s^{-1}. Taking into account the previously-established scaling, these velocities are significant with regard to accurately estimating K_x using ^{223}Ra and ^{224}Ra. Conversely, cross-shelf velocities measured throughout the water column during February and April were not significantly different than zero. It is possible that, during January, K_x values calculated using the exponential model (which

equates to a constant-depth mixed layer) overestimate the actual eddy diffusivity. However, this is not a problem for K_x values estimated using the variable-depth model, which takes the entire water column into consideration.

The total benthic radium flux is a combination of two components: radium produced in the sediments and diffused upward into the water column, and radium-enriched groundwater discharged directly into the ocean. While the benthic radium input was not directly measured during this study, the scale of this term can be evaluated by considering the sediment substrate and results from previous studies. Beck *et al.* (2008) report diffusive benthic fluxes of 4×10^{-5} dpm m^{-2} s^{-1} ^{223}Ra and 6×10^{-4} dpm m^{-2} s^{-1} ^{224}Ra to Great South Bay, a shallow embayment located north of the study area. While these fluxes are near (or at, in the case of ^{224}Ra) the aforementioned threshold magnitude, it is likely that diffusive benthic radium fluxes along the transect are lower. Hancock *et al.* (2006) previously linked diffusive radium fluxes to fine-grained terrigenous sediment, which is primarily deposited in nearshore areas and decreases in abundance with increasing offshore distance. Such fine-grained terrigenous material should be more highly concentrated in Great South Bay than in the MAB, where the surface sediment consists primarily of coarse-to-medium-grained quartz sand (Palmer and Lear, 1973). These type of sands are not regarded as a significant source of radium isotopes (e.g. Moore, 2003; Lamontagne *et al.*, 2008). The diffusive benthic radium flux to the study area, therefore, is likely insignificant in comparison to the eddy diffusion term.

The ^{223}Ra and ^{224}Ra supplied from submarine groundwater discharge can be approximated using information from the nearby South Atlantic Bight (SAB). Moore (2000) estimates that the average groundwater input to the SAB's inner shell ($\leq$20 km from shore) is $\sim$5L m^{-2} d^{-1}. Both analytical models (McBride and Pfannkuch, 1975; Bokuniewicz, 1992) and field studies (Bokuniewicz, 1980; Cable *et al.*, 1997; Taniguchi *et al.*, 2003) have demonstrated that groundwater discharge generally decreases with increasing offshore distance, however, suggesting that this level of discharge is not maintained across the entire shelf. Discharge can be approximated using an exponential equation,

$$J(x) = J_0 e^{-bx}, \tag{10}$$

where $J(x)$ is the groundwater flux density at offshore distance x, J_0 is the groundwater discharge at the shoreline, and b is a constant that determines the shape of the curve $J(x)$. While this exponential model is an oversimplification of the behavior of groundwater discharge in coastal regions, and does not account for the discontinuous nature of groundwater discharge on the shelf (e.g. Bratton, 2010), it can be used here to provide a rough approximation for the overall scale of groundwater discharge in the study area. From Eq. (10), if the average groundwater discharge $\bar{J}$ over a total distance from shore x' is known, and J_0 is estimated, b can be determined by integrating Eq. (10):

$$\int_0^{x'} J_0 e^{-bx} dx = \bar{J} x'. \tag{11}$$

The b term can be solved for iteratively, and groundwater discharge at specific distances from shore can subsequently be calculated using Eq. (10). Using Moore's values for $\bar{J}$ and x' (5L m^{-2} d^{-1} and 20 km, respectively), and a J_0 of 20L m^{-2} d^{-1}, discharge at offshore distances comparable to those of the MAB study area would fall between 0.4 and 0.001L m^{-2} d^{-1}. Higher values for discharge at the shore, such as the 50L m^2 d^{-1} measured by Bokuniewicz (1992) in Great South Bay, New York, would necessitate even lower discharge rates for the study area. This being the case, minimum ^{223}Ra and ^{224}Ra groundwater activities of 860 dpm 100L^{-1} and 12,000 dpm 100L^{-1} would be required to meet the threshold benthic flux value of 6×10^{-4} dpm m^{-2} s^{-1}. These activities are considerably higher than those measured in the coastal groundwater of nearby areas, such as southern Rhode Island's salt ponds (Hougham and Moran, 2007), Great South Bay (Beck *et al.*, 2008), and the Elizabeth River estuary (Charette and Buesseler, 2004). The minimum groundwater ^{224}Ra activity is also greater than the highest value reported for Southern New Jersey's Kirkwood-Cohansey aquifer (3730 dpm 100L^{-1}, Szabo *et al.*, 2004). It is probable, therefore, that the advective benthic flux term is also small in comparison to the eddy diffusion term, and can be disregarded in this study.

The groundwater discharge rates estimated using Eq. (10) do not take into account the advective transport through the sediment that occurs as a result of bottom currents and surface waves. Such flow has previously been observed in the coarse-grained MAB deposits at depths of $\leq$4.5 cm in the sediment (Reimers *et al.*, 2004). In order for this transport mechanism to provide a considerable radium flux, however, the shallow nature of this flow would require the upper sediment in the MAB to provide a large source of radium to the advected water. As previously noted, this is not the case here. Quartz sands, the primary sedimentary component in the MAB, are relatively radium-poor. Once again, it appears that the benthic flux term is negligible in comparison to eddy diffusion.

More generally, a large benthic flux of radium would be reflected in the CTD data. While a high ^{223}Ra-sample was collected near the seafloor in January (Fig. 5), this sample is located $>$100 km from shore, which is well offshore of where the gradient in surface ^{223}Ra is present. There are additional slight elevations in near-bottom ^{224}Ra activity present in each month's depth sections, but these activities are only marginally higher than the surrounding waters and, as with the high^{223}Ra sample, are found offshore of where the surface ^{224}Ra activity gradient exists. As a result, any potential benthic radium flux associated with this data does not have an effect on the K_x values calculated using the surface ^{223}Ra and ^{224}Ra gradients.

An additional assumption behind both the constant and variable-depth models is that along-shelf ^{223}Ra and ^{224}Ra gradients are inconsequential; both models are one dimensional, and a significant along-shelf gradient would require a two-dimensional approach. The effect of along-shelf variations in ^{223}Ra and ^{224}Ra activity on the K_x estimates here cannot be directly quantified because the along-shelf radium distribution was not measured. Nonetheless, this parameter can be estimated given the distance between the study area and the Hudson River Estuary, which is the nearest significant source of radium in the direction

perpendicular to the transect. Using the previously described scaling, a current of 5 cm s^{-1} would be sufficient for advection to outweigh eddy diffusion in the radium mass balance. Along-shelf velocities of this magnitude and greater were observed during the study period (Decker, 2009). The Hudson River estuary is located roughly 150 km away from the study area, and water advected at a constant velocity of 5 cm s^{-1} would take 34.7 d to travel this distance. After this amount of time, 87.9% of the ^{223}Ra and 99.9% of the ^{224}Ra initially present in the water originating from the Hudson River estuary will have decayed away. The highest nearshore ^{223}Ra and ^{224}Ra activities observed by Moore (2000) in the South Atlantic Bight are on the order of 4 dpm 100L^{-1} and 25 dpm 100L^{-1}, respectively. If ^{223}Ra and ^{224}Ra activities in the Hudson estuary are similar to these values, roughly 0.5 dpm 100L^{-1} ^{223}Ra and 0.04 dpm 100L^{-1} ^{224}Ra could be contributed to the study area from a direction roughly perpendicular to the transect. While it appears that there may be enough ^{223}Ra remaining to have an effect on K_x estimates here, this simple calculation does not take mixing, which would further dilute the radium contribution from the Hudson River estuary, into account. It is likely that a significant amount of mixing between water originating from the estuary and ambient shelf water occurs, and, subsequently, along-shelf contributions of ^{223}Ra and ^{224}Ra are negligible. This is not the case for the longer-lived ^{226}Ra and ^{228}Ra, however, as addressed later in the study.

c. ^{223}Ra and ^{224}Ra-based K_x estimates

During each month, total ^{224}Ra activity decreases rapidly within <40 km from shore before approaching a stable, nonzero level (Fig. 4). The latter activity, which varies temporally from a high of 1.6 dpm 100L^{-1} in February to a low of 1.1 dpm 100L^{-1} in April, is maintained over the bulk of the central and offshore portions of the transect. This apparent asymptote is not solely the consequence of supported ^{224}Ra. Average supported ^{224}Ra activities measured over the three cruises range from 0.4 ± 0.2–0.8 ± 0.5 dpm 100L^{-1}; these results are in approximate agreement with those of Kaufman *et al.* (1981), who report an average ^{228}Th (^{224}Ra's parent) activity of 0.5 ± 0.2 dpm 100L^{-1} for a similar transect off the coast of New Jersey. It is likely, therefore, that these nonzero activities represent the sum of supported ^{224}Ra and some background contamination from the sampling apparatus. Notably, this background activity cannot have originated from the ship's intake, as was the case for Charette *et al.* (2007), because it is also present in CTD samples. The stable nature of the total ^{224}Ra activity over the central and offshore portions of the transect, combined with the lack of a relationship between supported ^{224}Ra and offshore distance, suggests that the background contamination occurs at a consistent level throughout the surface transects. Consequently, the sum of the background ^{224}Ra and the supported ^{224}Ra is treated as a blank. The total ^{223}Ra surface distribution observed during each cruise exhibits a somewhat similar pattern to total ^{224}Ra (Fig. 4); following an initial steep decrease in activity, total ^{223}Ra approaches a nonzero value. It is assumed that, as with ^{224}Ra, this nonzero value represents the sum of supported ^{223}Ra and background contamination from the sampling

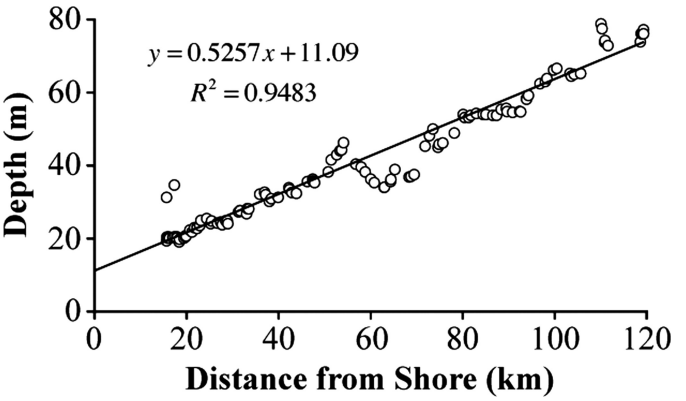

Figure 6. Depth soundings (open circles) acquired along the transect. The solid line through the data represents the best-fit linear solution for the bottom slope.

apparatus. Once again, this sum is treated as a blank. However, total ^{223}Ra does not maintain a consistent level in the area offshore of where the initial steep total ^{223}Ra gradient is present. Abrupt changes in total ^{223}Ra activity occur over the central and offshore portions of each cruise's surface transects (Fig. 4). Provided that contamination from the sampling apparatus is consistent, these shifts in ^{223}Ra activity can be attributed to changes in supported ^{223}Ra. The implications of these abrupt shifts in supported ^{223}Ra are addressed later in the discussion. For the purposes of the K_x calculations, supported ^{223}Ra levels inshore of 60 km are assumed to be constant.

As both ^{223}Ra and ^{224}Ra gradients are confined to within 60 km from shore, only data within this offshore distance was taken into consideration in the K_x calculations. Correspondingly, *unsupported* ^{223}Ra and ^{224}Ra activity is defined here as the total activity minus the blank (representing the sum of supported radium and contamination from the sampling apparatus) observed at 60 km from shore. ^{223}Ra and ^{224}Ra-based cross-shelf eddy diffusivities were determined by fitting Eqs. (3) and (5) to the surface unsupported dissolved radium data in a least-squared manner for two parameters (K_x and A_0). When two lines of radium activity were measured, as in January and February, these K_x estimates were calculated using the combined data from both transects. Additionally, cross-shelf eddy diffusivities were obtained from composite ^{223}Ra and ^{224}Ra radium activity data smoothed using a 5-point moving average and from radium data averaged into 5-km bins in order to evaluate the effect (if any) of data processing on K_x estimates. The variables α and H_0 used in Eq. (5) were based on a linear fit of depth sounding data acquired along the transect (Fig. 6).

Uncertainty in the estimated K_x values was calculated by smearing each month's activity data via a Monte Carlo technique. Using MATLAB (v. 7.3.0 R2006b), two series (r_a, r_b) of 500 random values between 0 and 1 were generated for every measured (offshore distance,

radium activity) point. A method developed by Box and Muller (1958) was then used to transform these randomly generated values into Gaussian deviates (z_a, z_b) as follows:

$$z_a = \sqrt{-2 \ln r_a} \cos 2\pi r_b$$
$$z_b = \sqrt{-2 \ln r_a} \sin 2\pi r_b. \tag{12}$$

The two series of random Gaussian deviates were then merged into a single array containing 1000 terms:

$$\{z_1, z_2, \ldots, z_{1000}\}. \tag{13}$$

Each of these deviates was used to obtain a random sample ($A'_{x,i}$) related to the radium activity measured at a specified location:

$$A'_{x,i} = \sigma z_i + A_x, \tag{14}$$

where A_x is the measured activity at location x, σ is the uncertainty associated with that activity, and the index i runs from 1 to 1000, covering the total number of Gaussian deviates previously generated. The uncertainty for each raw data point is related to the counting error, as described in the methods section, while σ for smoothed and binned data is equal to the standard error of the mean for each averaged point. In this manner, 1000 different activities were generated for each location, and the generated activities fit into a Gaussian distribution based on the measured activity and uncertainty in activity at that location. Eqs. (3) and (5) were fit to each indexed set of activity data, i.e.

$$\{A'_{x_1,1}, A'_{x_2,1}, \ldots, A'_{x_n,1}\}, \tag{15}$$

so that 1000 K_x estimates were produced for both the constant-depth and variable-depth models. The standard deviation of these estimates was used as the uncertainty for the K_x values determined from the measured radium data.

K_x estimates based on raw unsupported ^{223}Ra data range from 0.1–1.6 $\times$ 10^2 m^2 s^{-1} for the variable-depth model and from 0.1–1.2 $\times$ 10^2 m^2 s^{-1} for the constant-depth model (Table 1.3). For ^{224}Ra, these estimates range from 1.7–2.2 $\times$ 10^2 m^2 s^{-1} and 1.4–1.8 $\times$ 10^2 m^2 s^{-1} for the variable- and constant-depth models, respectively. Uncertainties range from $\pm$29–153% for raw ^{223}Ra-based estimates and from $\pm$15–27% for K_x values based on raw ^{224}Ra data; ^{224}Ra-based eddy diffusivities are more precise than those calculated using ^{223}Ra, due to the latter isotope's lower activity and its resultant higher relative measurement error. The large difference between ^{223}Ra and ^{224}Ra activities in seawater is ultimately tied to the ^{235}U/^{232}Th ratio in sediments, which ranges between 0.03–0.06 (Moore and Arnold, 1996). In every case, the constant-depth model produces lower K_x estimates than the variable-depth model. This trend is qualitatively consistent with the results reported by Hancock *et al.* (2006) which, at this time, provide the only other comparison between

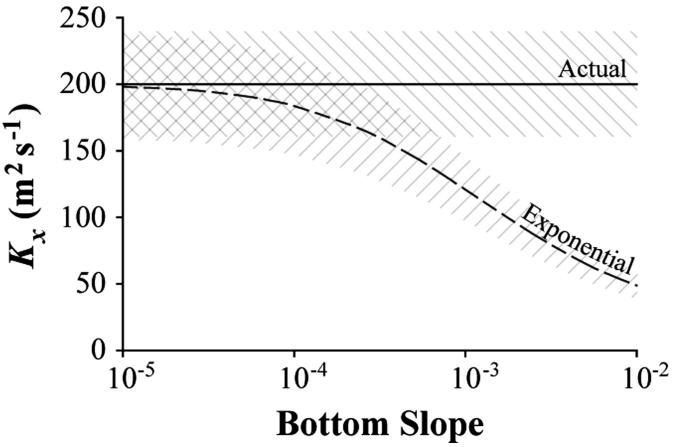

Figure 7. Departure of K_x estimates determined using the constant-depth (exponential) model (dashed line) from actual K_x values (solid line) as the bottom slope increases. In this example, the actual eddy diffusivity is set to 200 m^2 s^{-1}, while the variable H_0 is held constant at 10 m. The areas shaded with diagonal lines represent ±20% uncertainty.

constant-depth and variable-depth radium-based models. In the Great Barrier Reef (GBR), K_x values determined using the constant-depth model were as much as 70% lower than those estimated using a different variable-depth model (Hancock *et al.*, 2006). The difference between the two models employed in the MAB is not as large, however. Constant-depth K_x estimates are a maximum of 25% and 19% lower for ^{223}Ra and ^{224}Ra, respectively, and, when uncertainties are taken into consideration, the range of estimates produced using the two models overlaps. The disparity between these two studies is related primarily to the difference in bottom slope between the MAB and the GBR. The GBR's bottom slope is much greater than that of the MAB, and, therefore, the MAB is comparatively closer to a section of constant depth. These two examples illustrate that, depending on the bottom slope, the choice of model used to estimate K_x may be important. The divergence between the actual eddy diffusivity and that estimated using the exponential model grows larger as the bottom slope increases (Fig. 7).

Different methods of data processing can be implemented to reduce random error and eliminate short-term fluctuations in a radium dataset. These methods, however, can potentially affect the eddy diffusivities calculated from a given radium distribution; raw data may yield different K_x values compared to smoothed or binned data. The influence of data processing on radium-based K_x estimates is demonstrated in this study by smoothing the ^{223}Ra and ^{224}Ra data using a 5-point moving average and by binning the data into 5-km sections. As expected, uncertainty is almost universally lower for K_x values obtained from both binned and smoothed data than it is for the estimates based on raw data (Table 3). While many of the eddy diffusivities determined using binned and smoothed data fall within the raw data-based K_x values' bounds of uncertainty, this is not universally true. It is apparent

Table 3. Eddy diffusivities determined using ^{223}Ra and ^{224}Ra activities.

Month	Raw Data	Smoothed Data	Binned Data
	^{223}Ra-based K_x ($\times 10^2$ m^2 s^{-1})		
Variable Depth (Bessel) Model			
January	1.6 ± 0.5	1.5 ± 0.2	0.8 ± 0.2
February	0.1 ± 0.05[a]	0.5 ± 0.2	0.3 ± 0.1
April	1.4 ± 2.1	0.5 ± 0.1	0.8 ± 0.3
Constant Depth (Exponential) Model			
January	1.2 ± 0.3	1.2 ± 0.1	0.7 ± 1.3
February	0.1 ± 0.04[a]	0.4 ± 0.1	0.3 ± 0.2
April	1.0 ± 1.0	0.4 ± 0.1	0.6 ± 0.7
	^{224}Ra-based K_x ($\times 10^2$ m^2 s^{-1})		
Variable Depth (Bessel) Model			
January	1.7 ± 0.3	1.3 ± 0.1	1.5 ± 0.2
February	1.7 ± 0.4	1.6 ± 0.1	2.2 ± 0.3
April	2.2 ± 0.6	1.7 ± 0.2	2.1 ± 0.5
Constant Depth (Exponential) Model			
January	1.4 ± 0.2	1.1 ± 0.1	1.3 ± 0.2
February	1.4 ± 0.3	1.4 ± 0.1	1.8 ± 0.2
April	1.8 ± 0.4	1.5 ± 0.2	1.7 ± 0.4

[a]If supported ^{223}Ra activity is defined as the activity at 65 km ($\sim$0.05 dpm 100L^{-1}) instead of the activity at 60 km from shore ($\sim$0.09 dpm 100L^{-1}), February's ^{223}Ra distribution yields K_x values of $1.7 \pm 1.5 \times 10^2$ m^2 s^{-1} (variable-depth model) and $1.2 \pm 0.9 \times 10^2$ m^2 s^{-1} (constant-depth model).

from this analysis that K_x estimates can vary due to data processing, although the magnitude of this variation depends upon a given location's radium isotope distribution.

Previous estimates of horizontal eddy diffusivities have been made for the MAB. Stommel and Leetmaa (1972) calculated a wintertime cross-shelf eddy diffusivity of 2.28×10^2 m^2 s^{-1} for this area by balancing the input of freshwater from rivers with its removal through eddy diffusion. Using quasi-Lagrangian drifters, Münchow and Garvine (1993) determined a cross-shelf dispersion coefficient of 2.30×10^2 m^2 s^{-1} offshore of the Delaware River estuary. Ullman *et al.* (2006) utilized drifters and CODAR-based currents on the New Jersey Shelf to yield K_x estimates of 1.79×10^2 and 1.44×10^2 m^2 s^{-1} during March 2003 and July 2004. Considering the overall uncertainty in these eddy diffusivity estimates, ^{224}Ra-based K_x values produced using both constant- and variable-depth models are in agreement with the range (1.4–2.3×10^2 m^2 s^{-1}) provided by prior studies. ^{223}Ra-based diffusivities for January and April also fall in line with this range, but February's ^{223}Ra-based K_x values are anomalously low. This discrepancy can be attributed to the difficulty in identifying a supported ^{223}Ra value during February. If, during this month, supported ^{223}Ra is defined as the total ^{223}Ra activity observed between 65 and 85 km from shore ($\sim$0.05 dpm 100L^{-1}), instead of the total activity at 60 km from shore ($\sim$0.09 dpm 100L^{-1}),

the ^{223}Ra distribution yields eddy diffusivities of 1.7×10^2 m^2 s^{-1} for the variable-depth model and 1.2×10^2 m^2 s^{-1} for the constant-depth model. These eddy diffusivities are in better agreement with both those determined using ^{224}Ra and past K_x estimates for the MAB.

The temporal variability in the ^{224}Ra-based K_x estimates is low; eddy diffusivity varies by a factor of <2 from January to April. As reported above, the K_x values from this study also differ little from estimates made for the MAB in different seasons, years, and decades, further indicating that K_x changes little over time. By comparison, the difference between the K_x values determined for the MAB and those reported for other areas is much larger than the temporal variability seen in the MAB. For example, K_x estimates for areas near Huntington Beach, California (Colbert and Hammond, 2007), Apalachee Bay, Florida (Moore, 2003), and the Crozet Islands (Charette *et al.*, 2007) are on the order of 1–40 m^2 s^{-1}, while values in the Southern Drake Passage are as high as 6.3×10^4 m^2 s^{-1} (Dulaiova *et al.*, 2009). Although K_x differs significantly between locations, its change over time, at least in the MAB, is quite small. The lack of variability in K_x values observed over the study period, combined with the similarity between this study's K_x values and past K_x estimates for the MAB, suggests that the dominant processes controlling horizontal eddy diffusion are consistent over monthly, yearly, and possibly decadal timescales.

d. Implications for mid-shelf fronts

The MSF in the study area is located between 74 and 96 km from shore, at distances well offshore from where gradients in unsupported ^{223}Ra and ^{224}Ra are present. While the ^{228}Ra gradient is visible around the front, ^{228}Ra distributions do not provide an accurate quantitative measure of horizontal eddy diffusivity; this isotope is not in steady state with respect to its mean lifetime, $1/\lambda$ (Moore, 1987). Consequently, it was not possible to determine K_x values for the area immediately surrounding the front. More quantitative information could be gleaned from ^{223}Ra and ^{224}Ra if these isotopes' activities were higher, and their gradients better defined, at the offshore distances relevant to the MSF. This, however, would require a larger K_x, a considerably higher A_0, and/or the front to be much closer to the shore. Nonetheless, radium isotope distributions in the MAB do yield some qualitative information about MSFs. Observations from the MAB differ from theoretical data corresponding to the tidal dispersion frontogenesis model (Ou *et al.*, 2003), suggesting that MSFs are formed by a different mechanism. Trends in ^{228}Ra and supported ^{223}Ra near the front are consistent with several interpretations, including varying cross-shelf mixing rates (e.g. Knauss *et al.*, 1978; Huh and Ku, 1998), and concentrated equatorward advection.

In the tidal dispersion (TD) front formation model (Ou *et al.*, 2003), a buoyancy source at the coast is balanced by a depth-integrated cross-shelf flux from tidal shear dispersion. The depth-integrated cross-shelf dispersion coefficient reaches a minimum at mid-shelf depths, due to the coefficient's inverse correlation to water depth. This minimum, in turn, gives rise to a maximum in the density gradient, thus forming a front at the mid-shelf. Radium isotope

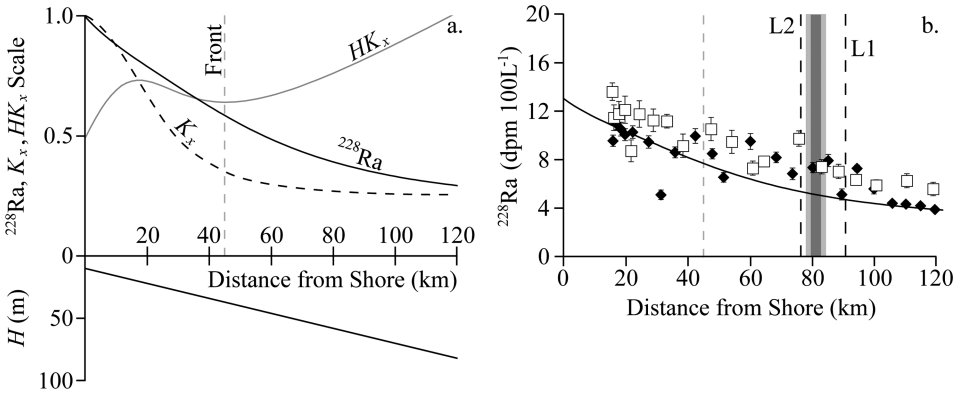

Figure 8. Theoretical ^{228}Ra distribution corresponding to the tidal dispersion (TD) frontogenesis mechanism (a) and actual ^{228}Ra data from the February cruise (b). The solid black line below the axis in Figure 8a depicts the modeled water depth (H). The dashed black curve and solid gray curve in Figure 8a correspond to eddy diffusivity (K_x) and depth-integrated eddy diffusivity (HK_x), respectively. The modeled front position is shown by the vertical dashed gray line. Scales for ^{228}Ra, K_x, and HK_x are 0–13 dpm 100L^{-1}, 0–41 m^2 s^{-1}, and 0–838 m^3 s^{-1}. Symbols depicting the instantaneous and cruise-averaged frontal positions in Figure 8b are retained from Figure 4, and the black curve in Figure 8b represents the modeled ^{228}Ra distribution corresponding to the TD mechanism.

distributions corresponding to this model were estimated by discretizing the steady-state form of Eq. (1) at 1.67-km intervals (corresponding to changes in water depth of 1 m) over an offshore distance of 1000 km. Advective and benthic input terms were disregarded. The resulting equation was treated as a two-point boundary value problem with known radium activities at the coastal and far-field boundaries and solved using MATLAB.

Cross-shelf eddy diffusivity values in this model were estimated using a derivation reported by Okubo (1967), in which horizontal shear dispersion is achieved by a constant vertical diffusivity and the sum of steady and oscillating (tidal) horizontal velocity components that vary linearly in the vertical direction. The surface cross-shelf tidal and steady velocities at the 50-m isobath used to calculate the K_x field here were set to 15 cm s^{-1} and 3 cm s^{-1}, respectively. These velocity values are based on a series of ADCP measurements taken during January and February of 2007 (D. S. Ullman, personal communication). The vertical diffusivity value used in the model (7.5×10^{-3} m^2 s^{-1}) was approximated, after Zimmerman (1986), as the product of the bottom drag coefficient (2×10^{-3}, Ou *et al.*, 2003) and the tidal transport at the 50-m isobath. The slope and intercept values used to determine water depth in this simulation were based upon depth soundings taken along the MAB transect (Fig. 6). The modeled ^{228}Ra distribution, given the boundary conditions $A = 10$ dpm 100L^{-1} at $x = 0$ and $A = 0$ at $x = 1000$ km, is illustrated in Figure 8, and is compared with ^{228}Ra data measured during February, when the front is most pronounced. To account for background ^{228}Ra from the open ocean, a value of 3.0 dpm 100L^{-1}, based

on the offshore Atlantic water activities reported by Key *et al.* (1985), was added to all calculated ^{228}Ra values. Adding this background value to the results, and not instead having a boundary condition of $A = 3.0$ dpm 100L^{-1} at $x = 1000$ km, ensures that the modeled data do not fall below observed open ocean ^{228}Ra activities at any point.

The modeled and observed data differ in several ways. ^{228}Ra activities measured during February vary slightly from the theoretical distribution; the TD model yields ^{228}Ra activities that are lower than the observed values over much of the line (Fig. 8). Furthermore, the MSF in this model is predicted to occur at 45 km from shore. This location is well inshore of where the front was actually observed during the study period (Table 1). In addition to these disparities, the maximum modeled K_x value ($41\ \text{m}^2\ \text{s}^{-1}$, Fig. 8) resulting from tidal shear dispersion is significantly lower than the eddy diffusivities determined using ^{223}Ra and ^{224}Ra in the MAB. Some of this discrepancy may be attributed to the omission of dispersion due to horizontal turbulence from the model. However, introducing a horizontal turbulent dispersion term of as little as $50\ \text{m}^2\ \text{s}^{-1}$ completely erases the mid-shelf depth-integrated K_x minimum needed to produce the front. These discrepancies between modeled and actual data suggest that the TD mechanism does not provide a comprehensive explanation for MSF frontogenesis.

Abrupt shifts in supported ^{223}Ra are present within 20 km of the 50-m isobath in each month's surface transects (Fig. 4). These patterns are indicative of reduced cross-shelf mixing, as mixing diminishes gradients. It is unclear, however, if the sharp transitions in supported ^{223}Ra are associated with the front. Although the front's position varies by as much as 15 km between surface transects sampled during each individual cruise, the location of the sudden changes in supported ^{223}Ra remains consistent over each month. These shifts in supported ^{223}Ra occur in close proximity (within $\sim$5 km) to the front's average position, as reported by Decker (2009). An abrupt transition in supported ^{223}Ra is only observed near the front's instantaneous location in April, when the instantaneous frontal position is also close to the average position. It is possible, therefore, that the supported ^{223}Ra distribution reflects a weekly-to-monthly average of oceanographic conditions. If this is the case, the shifts in supported ^{223}Ra indicate that MSFs may impede cross-shelf mixing.

In January and April, ^{228}Ra activities calculated using ^{223}Ra and ^{224}Ra-based K_x values fall below the ^{228}Ra activities measured over the central portion of the transect (Fig. 4). There are several potential reasons for this inconsistency. One possibility is that multiple mixing regimes exist within the study area. Because of its longer half-life, unsupported ^{228}Ra is present at greater distances from shore than shorter-lived unsupported ^{223}Ra and ^{224}Ra. Enhanced mixing offshore of the observed ^{223}Ra and ^{224}Ra gradients would not change the K_x values determined using these two isotopes, but would yield higher than expected ^{228}Ra values. While ^{228}Ra may not yield quantitative estimates of K_x, changes in mixing regimes have been observed using ^{228}Ra in previous studies (Knauss *et al.*, 1978; e.g. Huh and Ku, 1998). On a qualitative level, steep slopes in ln ^{228}Ra-versus-offshore distance can be associated with low rates of cross-shelf mixing, while shallow slopes can be linked to higher mixing rates. Using this rationale, January's ^{228}Ra data suggests that more rapid

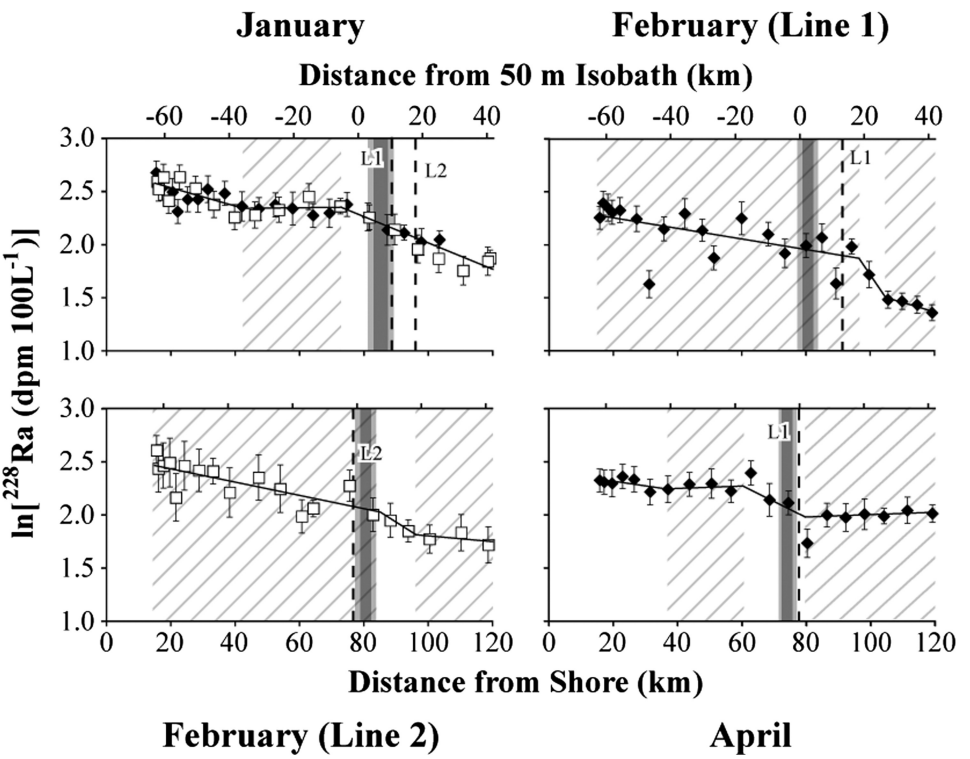

Figure 9. Plots of ln ^{228}Ra versus offshore distance. Changes in the ln(^{228}Ra)-versus- distance slope potentially reveal varying mixing regimes along the transect. Symbols representing data from the first and second lines, as well as those for the front's position, are retained from Figure 4. Solid lines fit through the data indicate the approximate ln(^{228}Ra)-versus distance gradient. Sections with comparatively high mixing rates are shaded with diagonal lines.

cross-shelf mixing occurs between 42–75 km from shore than between 0–42 and 75–120 km from shore (Fig. 9). Likewise, April's ^{228}Ra distribution could be caused by relatively high mixing rates between 36–60 and 80–120 km from shore, combined with lower cross-shelf mixing rates between 0–36 and 60–80 km from shore. Even during February, when the ^{228}Ra distributions estimated using ^{223}Ra and ^{224}Ra-based eddy diffusivities do not fall significantly below measured activities, there is evidence for varying mixing regimes along the transect. Plots of ln ^{228}Ra-versus offshore distance from this month are consistent with relatively low mixing rates between offshore distances of roughly 94–105 km during line 1 and 85–96 km during line 2 (Fig. 9).

As with the shifts in supported ^{223}Ra, these apparent changes in cross-shelf mixing cannot be definitively tied to the MSF. Both the front's average and instantaneous positions coincide with a steep ln -^{228}Ra gradient in January and April. However, the front lies inshore of an apparent low-mixing regime in February, when the MSF is strongest and most defined. These

relatively sharp ln -^{228}Ra gradients, therefore, may be related to a different oceanographic process. Consequently, the ^{228}Ra distribution does not provide conclusive evidence as to how the MSF affects cross-shelf mixing. Along-shelf transport also likely contributes to the observed ^{228}Ra distribution, further complicating the interpretation of these results.

An equatorward jet occurs near the surface coincident with the front. Its velocity varies over time (Table 2) in a pattern similar to the front's density step and gradient. The jet could cause ^{228}Ra activities to exceed projected values by advecting high-^{228}Ra water into the study area. This is to be expected, given the direction of the jet and the location of coastal radium sources surrounding the MAB. Radium activities are generally high near the shoreline due to desorption from particles and groundwater discharge (Moore, 2000). The bight is bordered by land to the north and west, and a large source of radium, the Hudson River estuary (Li and Chan, 1979), is located northwest of the study area. The Hudson Canyon, located to the north of the study area, may also provide a source of radium to MAB waters; submarine canyons can act as pathways for SGD (e.g. Person *et al.*, 2011). Consequently, both west-east and north-south long-lived radium activity gradients should exist in the MAB, and a jet advecting water from the north would move relatively high-activity water into the study area. In addition, eddy diffusion would spread radium from the jet laterally in a cross-shelf direction, resulting in higher than expected activities over an extended portion of the transect.

Depth sections of both ^{226}Ra and ^{228}Ra are consistent with this qualitative interpretation. Elevated ^{226}Ra and ^{228}Ra activities were observed near the surface in January and February's depth sections (Fig. 5) in an area roughly coincident with the jet's average position during these two months. This pattern of enrichment is not present, however, in April's data. Decker (2009) notes that the jet is difficult to distinguish at this time; although April's jet velocities are higher than those recorded during January, the intensification relative to the along-shelf velocity elsewhere along the transect is lower. The relationship between the jet and high ^{226}Ra and ^{228}Ra is consistent with the advection of radium-rich water from the north into the study area. Even so, the jet is not solely responsible for the discrepancy between predicted and measured ^{228}Ra activities. ^{228}Ra activities measured along the surface transects are not significantly above expected values during February, when the jet is strongest. Conversely, higher than expected ^{228}Ra activities are present over the center of the transect during April, even though the jet is nearly non-existent at this time. Both the jet and changing mixing regimes likely play a role here.

The ^{226}Ra and ^{228}Ra enrichment associated with the jet in the depth sections is much greater than that observed in the surface transects (Fig. 10). While it is unclear why this discrepancy exists, it is possible that cross-shelf mixing upstream of the study area, the source of radium to the jet, or the radium activity at the source of radium to the jet varies over short (daily-weekly) timescales; depth sections and surface transects were sampled at different times. Varying mixing rates will affect the degree to which high-activity source water is replaced by lower activity shelf water upstream of the study area. Changes in the location of the radium source, or in the source's radium activity, will also have a direct effect

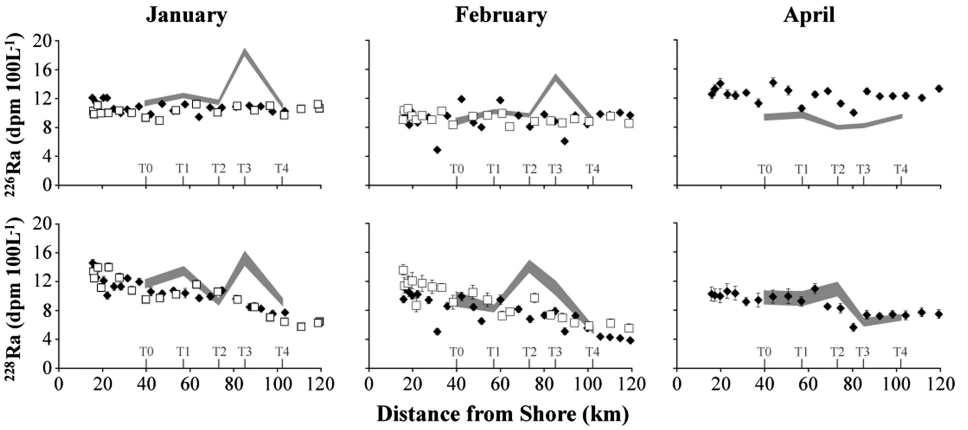

Figure 10. Discrepancy between surface ^{226}Ra and ^{228}Ra samples collected during long line transects (filled and open symbols) and those obtained during CTD depth section sampling (gray shaded area). Lines marked T0-T4 represent CTD sampling locations. The gray area representing CTD data encompasses the average and standard deviation of CTD ^{228}Ra activity.

on the high-Ra water that is transported in the jet. The discrepancy between ^{226}Ra and ^{228}Ra activities sampled along the long line transects and those from the depth sections would require increased mixing north of the study area and/or lower source radium activity during long line surface sampling. This explanation runs counter to evidence (described in Section 4c.) that K_x in the MAB is temporally constant, however. Additionally, the likelihood that only the CTD sections coincide with reduced mixing/higher source radium is low. It is doubtful, therefore, that temporal variability in either mixing rates or in the radium activity at the jet's source is responsible for the discrepancy between depth section and long line transect surface ^{226}Ra and ^{228}Ra activities.

Another possibility is that a significant portion of the radium in the jet is in particulate form; unlike samples collected along the surface transect, depth section samples were not filtered to remove particulate matter. This is unlikely, though, because an extremely high particle load would be required to contribute the necessary radium activity. In January, the difference between CTD and surface transect ^{226}Ra activity observed in the jet is $\sim$7 dpm 100L^{-1}. Given a ^{226}Ra activity of 1.8 dpm g^{-1} for suspended sediments (Li *et al.*, 1977), a suspended particulate matter (SPM) concentration of 39 mg L^{-1} would be required to account for this discrepancy. In comparison, the highest SPM value observed in the MAB by Kaufman *et al.* (1981) is 0.5 mg L^{-1}. The enormous difference between these two suspended particulate matter concentrations provides evidence that particulate radium cannot explain the divergence between depth section and surface transect radium values. Additionally, high particle concentrations would likely contribute significant ^{224}Ra activities to the depth section. ^{224}Ra regenerates at a faster rate than ^{228}Ra. As a result, ^{224}Ra enrichment due to particles would be expected to exceed the ^{228}Ra enrichment; this is not the case here.

The manner in which samples were collected may also contribute to the discrepancy between surface transect and CTD station ^{226}Ra and ^{228}Ra activities. As the long-line surface samples were collected while the ship was in motion, each sample reflects the average radium activity for roughly 2-km segments of the transect. Conversely, CTD surface samples were collected while the ship held its position at individual CTD stations, and these samples represent the radium activity at a single point. It is possible that, in the surface transects, the high ^{226}Ra and ^{228}Ra activity water from the jet is diluted with lower activity water surrounding the feature during collection, thus reducing the jet's prominence in surface transect data. However, this explanation would require the jet to be much narrower than the ~2-km window over which surface transect samples were collected. Provided that the width of the jet is similar to that of the front, this is likely not the case; Decker (2009) reports average frontal widths ranging from $3.0 \pm 0.5 - 4.5 \pm 0.8$ km. Furthermore, if the jet's width was significantly less than 2 km, the CTD stations would have to fall precisely in line with the feature in order to capture its high radium activity signal. Given the temporal variability in the front's position (Table 1), this is unlikely. It is still unclear, therefore, why ^{226}Ra and ^{228}Ra activities associated with the jet in the CTD data greatly exceed those observed in the surface transects.

Although, in the study area, the long-lived radium isotopes are enriched within the jet, ^{223}Ra and ^{224}Ra activities do not exceed those in the surrounding waters. Sources of ^{226}Ra and ^{228}Ra to the coastal ocean also tend to have high ^{223}Ra and ^{224}Ra activities. The absence of short-lived radium here indicates that the source of radium to the jet lies far enough away from the study area for the latter two isotopes to decay to background levels. The distance between the source of radium to the jet and the study area can be estimated using a two end-member mixing model:

$$^{224}Ra_j = f\,^{224}Ra_s \exp(-\lambda_{224} t_s) + (1 - f)\,^{224}Ra_o \exp(-\lambda_{224} t_o), \tag{16}$$

where ^{224}Ra is the unsupported activity measured (or estimated) in the jet and the two end-members, f is the fraction of water in the jet originating from the radium source, and t is the age of the water originating from each end-member. This age is defined as the time since water from the given end-member was mixed into the jet. The subscripts j, s, and o refer to the jet, the radium source, and the ocean water surrounding the jet, respectively. Given the assumptions that $^{224}Ra_j \approx {}^{224}Ra_o$ (as is the case within the study area) and $t_s \approx t_o$ (assuming that $t_s \approx t_o$ yields a low-end estimate for t_s; it is likely that t_o is less than t_s), Eq. (16) can be rewritten as:

$$t_s \approx \frac{\ln\left[f(R_{224}^{-1} - 1) + 1\right]}{\lambda_{224}}. \tag{17}$$

Here, R_{224} represents the ratio of unsupported ^{224}Ra activity observed in the jet to that initially present at the source. If the jet's velocity, v, is constant, the distance, y (where $y = vt_s$), between the study area and the source of radium to the jet can subsequently be

Table 4. Data used to estimate the distance between the study area and the source of radium to the alongshelf jet.

	January	February
$^{226}Ra_j$ (dpm 100L^{-1})	18	15
$^{226}Ra_s$ (dpm 100L^{-1})	30	30
$^{226}Ra_o$ (dpm 100L^{-1})	11	10
f	0.37	0.25
R_{224}	0.03	0.03
v (cm s^{-1})[a]	6	31
y (km)	69	303

[a](Decker, 2009)

determined by multiplying Eq. (17) by v. This distance can also be estimated using ^{223}Ra; because of its shorter half-life, ^{224}Ra provides a lower, more conservative, estimate for y.

The f parameter in Eq. (17) can be approximated using another simple mixing model:

$$^{226}Ra_j = f^{226}Ra_s + (1 - f)^{226}Ra_o, \tag{18}$$

where ^{226}Ra represents ^{226}Ra activity. If the source of radium to the jet originates from radium-enriched surface water, $^{226}Ra_s$ likely is below 30 dpm 100L^{-1}. Surface water ^{226}Ra activities measured in the nearby South Atlantic Bight (Moore, 2000) and in coastal areas near Long Island (Beck *et al.*, 2008) do not exceed this value. Given the ^{226}Ra activities observed within and surrounding the jet (Table 4), f is greater than 0.37 and 0.25 in January and February, respectively, providing the radium source is from surface water.

Unsupported ^{224}Ra activities in the jet within the study area are negligible. Because radium isotopes are below detection levels after decay equivalent to 5 half-lives, the ratio of measured to initial ^{224}Ra activity can be set to 0.03. It is likely even lower than this value; $R_{224} = 0.03$ is used to provide a conservative estimate for y. The average jet velocities recorded during the January and February cruises are 6 cm s^{-1} and 31 cm s^{-1}, respectively (Decker, 2009). Using these values and Eq. (17), the distance from the radium-enriched source to the study area is on the order of 71 km in January and 315 km in February (Table 4). As the Hudson River estuary lies approximately 150 km north of the study area, this suggests that the jet associated with the MSF provides a pathway to effectively transport chemicals from the estuary downshelf into the MAB. If the radium source originates from a localized groundwater input with ^{226}Ra activity much higher than 30 dpm 100L^{-1}, it is possible that these distances are shorter (Fig. 11). However, this would require an extremely low groundwater ^{224}Ra/^{226}Ra ratio ($\ll$1). This ratio is almost universally greater than one in groundwater samples taken in areas surrounding the MAB (Charette *et al.*, 2001; Szabo *et al.*, 2004; e.g. Beck *et al.*, 2008), making local groundwater an unlikely source of radium to the jet.

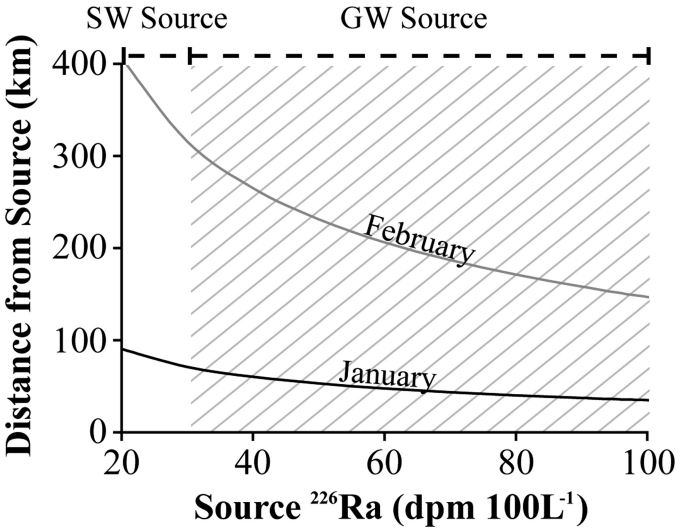

Figure 11. Jet transport model depicting the relationship between the radium activity in the jet's source water and the distance between the study area and the source. Results are calculated using Eqns. (17) and (18) with data from Table 4. If the source of radium to the jet originates from surface water ($<$30 dpm ^{226}Ra 100L^{-1}), the distance from the study area to the jet is greater than 70 km in January (black line) and 300 km in February (gray line). These distances decrease if groundwater ($\geq$30 dpm ^{226}Ra 100L^{-1}) is the primary source of radium to the jet.

5. Conclusions

Radium isotope distributions in the MAB provide constraints on local eddy diffusivities, and offer new insight into mid-shelf front dynamics. When variable water depth is accounted for, eddy diffusivities determined using ^{223}Ra and ^{224}Ra range from 0.1–1.6 $\times$ 10^2 m^2 s^{-1} and 1.7–2.2 $\times$ 10^2 m^2 s^{-1}, respectively. The relative uncertainty for ^{223}Ra-based values ($\pm$37–169%) is considerably higher than that of those estimated using ^{224}Ra ($\pm$16–28%), due primarily to the former isotope's lower observed activities and corresponding higher counting error. Nondimensional scaling reveals that advection and benthic radium input do not have a significant effect on these eddy diffusivity estimates. Temporal variability in eddy diffusivities calculated over the three months is low in comparison to the uncertainty of these values. Combined with the similarity between the eddy diffusivities from this study and past values calculated for the MAB (e.g. Stommel and Leetmaa, 1972; Münchow and Garvine, 1993; Ullman *et al.*, 2006), these results suggest that K_x is relatively constant over months, years, and perhaps even decades.

Observations from the MAB differ from theoretical data corresponding to Ou *et al.'s* (2003) tidal dispersion frontogenesis mechanism. This mechanism, therefore, does not provide a comprehensive description for MSF formation. Abrupt shifts in supported ^{223}Ra and changes in the ^{228}Ra gradient occur in close proximity to the front. These trends, if caused

by the front, indicate that MSFs impede cross-shelf mixing. While cross-shelf mixing may be inhibited by the front's presence, transport in the along-shelf (equatorward) direction is almost certainly enhanced. ^{226}Ra and ^{228}Ra are enriched within the equatorward jet associated with the front, and the absence of unsupported ^{223}Ra and ^{224}Ra in the jet indicates that the source of radium to the jet lies on the order of hundreds of km from the study site. The jet associated with the MSF provides a pathway to effectively transport chemicals from the Hudson River estuary over large distances down-shelf.

The radium quartet, while providing important general constraints on mixing in the MAB, cannot be used here to conclusively determine the front's effect on cross-shelf mixing. The observational limitations arise as a result of ^{223}Ra and ^{224}Ra not being ideally tuned to the offshore distances relevant to the MSF in the study area. ^{223}Ra and ^{224}Ra potentially have greater utility in regions where the MSF is closer to shore or where K_x is considerably higher. Moreover, a longer-term (year-long) observation of radium activities would provide additional information about the front's effect on cross-shelf mixing. Because the front persisted throughout the study period, a comparison could not be made between the radium isotope distributions measured during this time and those from when the front is absent. Consequently, the abrupt shifts in ^{223}Ra and changes in the ^{228}Ra gradient observed near the front, which are indicative of reduced cross-shelf mixing, could not be definitively linked to the MSF. These results provide new information on the utility and limitation of these tracers in evaluating cross-shelf mixing and mid-shelf front-related processes.

Acknowledgments. We thank the captain and crew of the *R/V Endeavor*, Art Spivack for his assistance with data error analysis, and J. Kirk Cochran and three anonymous reviewers for their constructive comments. Funding for this project was provided by the NSF (OCE-0550770) and RI Sea Grant.

REFERENCES

Beck, A. J., J. P. Rapaglia, J. K. Cochran, H. J. Bokuniewicz and S. Yang. 2008. Submarine groundwater discharge to Great South Bay, NY, estimated using Ra isotopes. Mar. Chem., *109*, 279–291.

Belkin, I. and M. Spall. 2002. New old frontier: ocean fronts. Dyn. Atmos. Ocean, *36*, 1–2.

Blanton, J. O. 1986. Coastal frontal zones as barriers to offshore fluxes of contaminants. Rapp. P.-V. Cons. Int. Explor. Mer., *186*, 18–30.

Bokuniewicz, H. J. 1980. Groundwater seepage into Great South Bay, New York. Estuar. Coast. Mar. Sci., *10*, 437–444.

—— 1992. Analytical descriptions of subaqueous groundwater seepage. Estuaries, *15*, 458–464.

Box, G. E. P. and M. E. Muller. 1958. A note on the generation of random normal deviates. Ann. Math. Stat., *29*, 610–611.

Bratton, J. F. 2010. The three scales of submarine groundwater flow and discharge across passive continental margins. J. Geol., *118*, 565–575.

Cable, J. E., W. C. Burnett and J. P. Chanton. 1997. Magnitude and variations of groundwater seepage along a Florida marine shoreline. Biogeochemistry, *38*, 189–205.

Chapman, D. C. and R. C. Beardsley. 1989. On the origin of shelf water in the Middle Atlantic Bight. J. Phys. Oceanogr., *19*, 384–391.

Charette, M. A. and K. O. Buesseler. 2004. Submarine groundwater discharge of nutrients and copper to an urban subestuary of Chesapeake Bay (Elizabeth River). Limnol. Oceanogr., *49*, 376–385.

Charette, M. A., K. O. Buesseler and J. E. Andrews. 2001. Utility of radium isotopes for evaluating the input and transport of groundwater-derived nitrogen to a Cape Cod estuary. Limnol. Oceanogr., *46*, 465–470.

Charette, M. A., M. E. Gonneea, P. J. Morris, P. Statham, G. Fones, H. Planquette, I. Salter and A. N. Garabato. 2007. Radium isotopes as tracers of iron sources fueling a Southern Ocean phytoplankton bloom. Deep-Sea Res., *54*, 1989–1998.

Colbert, S. L. and D. E. Hammond. 2007. Temporal and spatial variability of radium in the coastal ocean and its impact on computation of nearshore cross-shelf mixing rates. Cont. Shelf Res., *27*, 1477–1500.

Decker, L. B. 2009. Mean thermohaline and velocity structure of the Mid-Atlantic Bight mid-shelf front. University of Rhode Island, Narragansett, RI, 62 pp.

Dulaiova, H., M. V. Ardelan, P. B. Henderson and M. A. Charette. 2009. Shelf-derived iron inputs drive biological productivity in the southern Drake Passage. Global Biogeochem. Cycles, *23*, GB 4014, doi:4010.1029/2008GB003406.

Hancock, G. J., I. T. Webster and T. C. Steiglitz. 2006. Horizontal mixing of Great Barrier Reef waters: offshore diffusivity determined from radium isotope distribution. J. Geophys. Res., *111*, 19–33.

Harms, I. H., M. J. Karcher and D. Dethleff. 2000. Modelling Siberian river runoff - implications for contaminant transport in the Arctic Ocean. J. Mar. Syst., *27*, 95–115.

Hill, A. E., I. D. James, P. F. Linden, J. P. Matthews, D. Prandle, J. H. Simpson, E. M. Gmitrowicz, D. A. Smeed, K. M. M. Lwiza, R. Durazo, A. D. Fox and D. G. Bowers. 1993. Dynamics of tidal mixing fronts in the North Sea. Philos. Trans. R. Soc. London, *343*, 431–446.

Hougham, A. L. and S. B. Moran. 2007. Water mass ages of coastal ponds estimated using ^{223}Ra and ^{224}Ra as tracers. Mar. Chem., *105*, 194–207.

Houghton, R. W. and M. Visbeck. 1998. Upwelling and convergence in the Middle Atlantic Bight Shelfbreak Front. Geophys. Res. Lett., *25*, 2765–2768.

Huh, C.-A. and T.-L. Ku. 1998. A 2-D section of ^{228}Ra and ^{226}Ra in the Northeast Pacific. Oceanol. Acta, *21*, 533–542.

Imboden, D. M. and S. Emerson. 1978. Natural radon and phosphorus as limnologic tracers: Horizontal and vertical eddy diffusion in Greifensee. Limnol. Oceanogr., *23*, 77–90.

Kaufman, A., Y.-H. Li and K. K. Turekian. 1981. The removal rates of ^{234}Th and ^{228}Th from waters of the New York Bight. Earth Planet. Sci. Lett., *54*, 385–392.

Key, R. M., J. L. Sarmiento and W. S. Moore. 1985. Distribution of Ra-228 and Ra-226 in the Atlantic Ocean, Technical Report, Ocean Tracer Lab, Princeton.

Knauss, K. G., T. L. Ku and W. S. Moore. 1978. Radium and thorium isotopes in the surface waters of the East Pacific and Southern California. Earth Planet. Sci. Lett., *39*, 235–249.

Koczy, F. F. 1958. Natural radium as a tracer in the ocean. Proc. 2nd Intern. Conf. Peaceful Uses At. Energy, *18*, 351–357.

Lamontagne, S., C. L. G. L. Salle, C. J. Hancock, I. T. Webster, C. T. Simmons, A. J. Love, J. James-Smith, A. J. Smith, J. Kämpf and H. J. Fallowfield. 2008. Radium and radon radioisotopes in regional groundwater, intertidal groundwater, and seawater in the Adelaide Coastal Waters Study area: Implications for the evaluation of submarine groundwater discharge. Mar. Chem., *109*, 318–336.

Laubscher, R. K., R. Perissinotto and C. D. McQuaid. 1993. Phytoplankton production and biomass at frontal zones in the Atlantic sector of the Southern Ocean. Polar Biol., *13*, 471–481.

Li, Y.-H. and L.-H. Chan. 1979. Desorption of Ba and ^{226}Ra from river-borne sediments in the Hudson estuary. Earth Planet. Sci. Lett., *43*, 343–350.

Li, Y.-H., G. Mathieu, P. Biscaye and H. J. Simpson. 1977. The flux of ^{226}Ra from estuarine and continental shelf sediments. Earth Planet. Sci. Lett., *37*, 237–241.

Linden, P. F. and J. E. Simpson. 1988. Modulated mixing and frontogenesis in shallow seas and estuaries. Cont. Shelf Res., *8*, 1107–1127.

List, E. J., G. Gartrell and C. D. Winant. 1990. Diffusion and dispersion in coastal waters. J. Hydraul. Eng., *116*, 1158–1179.

Marra, J., R. W. Houghton and C. Garside. 1990. Phytoplankton growth at the shelf-break front in the Middle Atlantic Bight. J. Mar. Res., *48*, 851–868.

McBride, M. S. and H. O. Pfannkuch. 1975. The distribution of seepage within lakebeds. J. Res. U.S. Geol. Survey, *3*, 505–512.

Moore, W. S. 1987. Radium 228 in the South Atlantic Bight. J. Geophys. Res., *92*, 5177–5190.

—— 2000. Determining coastal mixing rates using radium isotopes. Cont. Shelf Res., *20*, 1993–2007.

—— 2003. Sources and fluxes of submarine groundwater discharge delineated by radium isotopes. Biogeochemistry, *66*, 75–93.

Moore, W. S. and R. Arnold. 1996. Measurement of ^{223}Ra and ^{224}Ra in coastal waters using a delayed coincidence counter. J. Geophys. Res., *101*, 1321–1329.

Mountain, D. G. 2003. Variability in the properties of shelf water in the Middle Atlantic Bight, 1977–1999. J. Geophys. Res., *108*, 1029–1044.

Münchow, A. and R. W. Garvine. 1993. Buoyancy and wind forcing of a coastal current. J. Mar. Res., *51*, 293–322.

Okubo, A. 1967. The effect of shear in an oscillatory current on horizontal diffusion from an instantaneous source. Int. J. Oceanol. Limnol., *1*, 194–204.

—— 1971. Oceanic diffusion diagrams. Deep Sea Res., *18*, 789–802.

Ou, H.-W., C.-M. Dong and D. Chen. 2003. Tidal diffusivity: a mechanism for frontogenesis. J. Phys. Oceanogr., *33*, 840–847.

Palmer, H. D. and D. W. Lear. 1973. Environmental survey of an interim ocean dumpsite: Middle Atlantic Bight, U.S. Environmental Protection Agency.

Perlanez, R. 2004. A particle-tracking model for simulating pollutant dispersion in the Strait of Gibraltar. Mar. Pollut. Bull., *49*, 613–623.

Person, M., B. Dugan, J. B. Swenson, L. Urbano, C. Stott, J. Taylor and M. Willett. 2011. Pleistocene hydrogeology of the Atlantic continental shelf, New England. Geol. Soc. Am. Bull., *115*, 1324–1343.

Peterson, R. N., W. C. Burnett, M. Taniguchi, J. Chen, I. R. Santos and S. Misra. 2008. Determination of transport rates in the Yellow River-Bohai Sea mixing zone via natural geochemical tracers. Cont. Shelf Res., *28*, 2700–2707.

Rasmussen, L. L. 2003. Radium isotopes as tracers of coastal circulation pathways in the Mid-Atlantic Bight. MIT/WHOI, 214 pp.

Reimers, C. E., H. A. Stecher III, G. L. Taghon, C. M. Fuller, M. Huettel, A. Rusch, N. Ryckelynck and C. Wild. 2004. In situ measurements of advective solute transport in permeable shelf sands. Cont. Sh. Res, *2004*, 183–201.

Somayajulu, B. L. K., M. M. Sarin and R. Ramesh. 1996. Denitrification in the eastern Arabian Sea: evaluation of the role of continental margins using Ra isotopes. Deep-Sea Res., *43*, 111–117.

Stommel, H. and A. Leetmaa. 1972. Circulation on the continental shelf. Proc. Nat. Acad. Sci. U.S.A., *69*, 3380–3384.

Sundermeyer, M. A. and J. R. Ledwell. 2001. Lateral dispersion over the continental shelf: analysis of dye release experiments. J. Geophys. Res., *106*, 9603–9621.

Szabo, Z., V. T. dePaul, T. F. Kraemer and B. Parsa. 2004. Occurrence of Radium-224, Radium-226, and Radium-228 in Water of the Unconfined Kirkwood-Cohansey Aquifer System, Southern New Jersey, U.S. Geological Survey.

Taniguchi, M., W. C. Burnett, C. F. Smith, R. J. Paulsen, D. O'Rourke, S. L. Krupa and J. L. Christoff. 2003. Spatial and temporal distributions of submarine groundwater discharge rates obtained from various types of seepage meters at a site in the Northeastern Gulf of Mexico. Biogeochemistry, *66*, 35–53.

Tintore, J., P. E. L. Violette, I. Blade and A. Cruzado. 1988. A study of an intense density front in the Eastern Alboran Sea: The Almeria-Oran Front. J. Phys. Oceanogr., *18*, 1384–1397.

Torgersen, T., K. K. Turekian, V. C. Turekian, N. Tanaka, E. DeAngelo and J. O'Donnell. 1996. ^{224}Ra distribution in surface and deep water of Long Island Sound: sources and horizontal transport rates. Cont. Shelf Res., *16*, 1545–1559.

Ullman, D. S. and P. C. Cornillon. 1999. Satellite-derived sea surface temperature fronts on the continental shelf off the northeast U.S. coast. J. Geophys. Res., *104*, 23459–23478.

—— 2001. Continental shelf surface thermal fronts in winter off the northeast US coast. Cont. Shelf Res, *21*, 1139–1156.

Ullman, D. S., J. O'Donnell, J. Kohut, T. Fake and A. Allen. 2006. Trajectory prediction using HF radar surface currents: Monte Carlo simulations of prediction uncertainties. J. Geophys. Res., *111*, doi: 10.1029/2006JC003715.

Wang, D.-P. 1979. Low frequency sea level variability on the Middle Atlantic Bight. J. Mar. Res., *37*, 683–697.

Wu, Y., R. Falconer and B. Lin. 2005. Modelling trace metal concentration distributions in estuarine waters. Estuar. Coast. Mar. Sci., *64*, 699–709.

Yoder, J. A., S. G. Ackleson, R. T. Barber, P. Flament and W. M. Balch. 1994. A line in the sea. Nature, *371*, 689–692.

Zimmerman, J. T. F. 1986. The tidal whirlpool: A review of horizontal dispersion by tidal and residual currents. Netherland. J. Sea. Res., *20*, 133–154.

Received: *6 May, 2011*; revised: *22 October, 2011*.